Prediction of rough-wall boundary layers using a low Reynolds number k–ε model

F. Tarada*
Thermo-Fluid Mechanics Research Centre, University of Sussex, Falmer, Brighton, East Sussex, UK

A low Reynolds number k–ε model applicable to flows over rough surfaces is reported in this article. A complementary roughness drag coefficient model that takes into account the isolated, wake interference and skimming roughness flow regimes is formulated and calibrated. It is based on a wide range of published experimental data concerning flow over *deterministic* roughness, comprising the data sets of Schlichting, Marshall, Gaudet, Zukauskas, and Scaggs *et al.* The model thus obtained provides good predictions for the enhancement of mixing lengths between hemispherical roughness elments as reported by Chen. Predictions of boundary-layer flow over *stochastically* rough surfaces were obtained by invoking three topographic models that require various roughness statistics as inputs. Predicted skin friction and transition location values for flows over the stochastically rough plates of Karlsson, Al-Shukri, Acharya *et al.*, and Watt were generally satisfactory.

Keywords: boundary layers; roughness; turbulence modeling

Introduction

Prediction of boundary-layer behavior over rough surfaces is a significant engineering problem that is both important and difficult to achieve with a sufficient degree of accuracy. Development of a reliable mathematical model for rough boundary-layer flow would be of tremendous value to engineers in the design of gas turbines, ships, and aircraft, all of which may be susceptible to both manufacturing roughness and in-service degradation of surface finish.

Current methods for the calculation of rough-wall boundary layers can be classified into three main categories:

(1) Correlations of the variation of skin friction coefficient and velocity shift (due to roughness) as functions of the equivalent "sand-grain" height, k_s (the latter term is in reference to Nikuradse's[1] rough pipe flow experiments). Examples of these correlations include those provided by Schlichting[2] and Colebrook and White.[3] These correlations are still widely used to provide first estimates of the likely effects of a given roughness level, but are unsuitable for extrapolation into roughness types other than those experimentally investigated and cannot represent the physics of rough, turbulent boundary layers.

(2) Momentum integral methods, which rely on empirical correlations for skin coefficient and boundary-layer entrainment to calculate the evolution of rough-wall boundary layers. These have been employed by Dvorak,[4] Dirling,[5] and Christoph,[6] among others. Although these methods enable the influence of streamwise pressure gradient to be taken into account, they still rely on empirical correlations of limited applicability.

(3) Differential methods, which solve for the Reynolds averaged boundary-layer equations to predict rough flows. These methods have the widest applicability of the three calculation methods. McDonald and Fish,[7] Cebeci and Chang,[8] and Ligrani *et al.*[9] used mixing-length formulations with enhanced van Driest damping factors in differential-type approaches to the problem of flow over rough surfaces. However, the flow *between* the roughness elements was not considered in their approaches. Finson *et al.*[10–14] used a Reynolds stress turbulence model to calculate rough-wall boundary layers, including a parabolic model of the flow between the roughness elements. A roughness sink term was introduced in the momentum equation to account for roughness drag, and source terms in the turbulent stress equations accounted for vortex shedding. However, despite its apparent sophistication, Finson's model suffers from inaccurate roughness blockage specifications and from the limited applicability of its roughness drag coefficients. Lin and Bywater's[15] and Christoph and Pletcher's[16] differential models, which employed mixing-length turbulence models, suffered the same problems. Taylor *et al.*[17] derived the correct roughness blockage expressions for roughness elements of circular cross section but used a simple mixing-length model that did not take roughness into account.

A summary of the roughness drag coefficients utilized by different investigators is presented in Table 1.

In this article, a differential model supplemented by a low Reynolds number k–ε turbulence model applicable to rough walls is presented and extensively calibrated over a wide range of published experimental data regarding *deterministic* roughness. The same model is then applied to a range of data pertaining to *stochastic* roughness.

The calculation methods relating to rough-wall boundary-layer flow are far easier to apply to *deterministic* roughness, where the dimensions of the roughness elements are known precisely, than to *stochastic* roughness, because the central question of how to characterize stochastic roughness has not been properly addressed to date. In the absence of such a characterization method, inspired guess-work seems to have been used in the past.

Finson[10] presented predictions of Feindt's[18] experimental data on transition due to sand grain roughness; conical and hemispherical topographies were employed with guessed dimensions. Finson and Clarke[13] also relied on "guesstimates"

* Currently with Mott MacDonald Consultants Ltd., 20/26 Wellesley Road, Croydon CR9 2UL, England
Address reprint requests to Dr. Tarada at the Thermo-Fluid Mechanics Research Centre, University of Sussex, Falmer, Brighton, East Sussex BN1 9QT, UK.

Received 10 May 1989; accepted 5 April 1990

Table 1 Summary of C_D proposals

Researchers	Turbulence model	C_D
Finson (1975)	Reynolds stress closure	0.5 for spheres 1.0 for cones
Lin and Bywater (1982)	One equation (turbulent kinetic energy)	Direct reading of Zukauskas[37] data
Christoph and Pletcher (1983)	Mixing length	0.5
Taylor *et al.* (1985)	Mixing length	$C_D = \max(0.6, 2.37\,\mathrm{Re}_d^{-0.125})$
Current investigation	Two equation (k–$\tilde{\varepsilon}$)	$C_D = \max[C_{DP}, C_{DP}(\mathrm{Re}_d/\mathrm{Re}_{dc})^{-0.289}] + 16(\beta_x^{-1}-1)/\mathrm{Re}_d$ $C_{DP} = \min\{0.182 + 0.0542/L_c^{1/2}, 1.1 - 0.7\exp[-0.597(H/\bar{D})^{0.419}]\}$ $\mathrm{Re}_{dc} = \min(4.35\times10^2/L_c^{1/2}, 5\times10^3)$

when attempting to predict experimental test cases of high Mach number flows over grit. Lin and Bywater[15] "postdicted" several rough-flow test cases by simply determining the optimum area blockage terms for the individual test cases considered.

Taylor *et al.*[17,19] presented equations for blockage factors and roughness source terms as ensemble averages of roughness diameters. However, their formulations do not make use of standard roughness parameters as measured by a profilometer instrument, nor is the question of how to automatically identify roughness "diameters" from two-dimensional (2-D) profiles of stochastic roughness adequately addressed.

Despite the difficulties involved in the characterization of stochastic roughness, it has become increasingly obvious to researchers that the only way we may hope to supersede nebulous "sand-grain" roughness concepts is to include extra information, beyond just a nominal roughness height, in any model describing roughness. For example, Grigson[20] states as one of his main conclusions in an extensive paper on roughness on ships' hulls that "the *quality* of the surface topography, affecting the shape of the Clauser function, is as important as the height of roughness in governing the viscous drag."

The philosophy behind the topographic models proposed here is that maximum use should be made of standard roughness parameters measured by commercial profilometers, namely, ordinate moment statistics (centerline average height, root-mean-square (rms) height, etc.) and profile slope statistics (mean absolute profile slope, root-mean-square (rms) angle, etc.) to fix the dimensions of two simple model topographies (truncated

Notation

C_D	Coefficient of drag based on local velocity
C_f	Skin friction coefficient
C_k	Constant defining roughness source term in k-equation
$C_{\varepsilon1}, C_{\varepsilon2}, C_{\varepsilon3}$	Turbulence "constants" in dissipation equation
$D(y)$	Diameter of roughness element at given height, y
$\bar{D}$	Average roughness diameter, $\frac{1}{H}\int_{y=0}^{H} D(y)\,dy$
D_0	Diameter at base of roughness element
f	Pipe friction factor, $2U_\tau^2/U_e^2$
f_μ	Low Reynolds number correction to turbulent viscosity
h	Melt-down height
H	Height of roughness element *or* boundary-layer shape factor
k	(Specific) kinetic energy of turbulence
L	Geometric mean roughness spacing $(L_xL_z)^{1/2}$
L_c	Roughness lateral cover, frontal area/total plan area $(=\bar{D}H/(L_xL_z))$
L_x, L_z	Roughness spacings in x and z directions
m_a	Arithmetic mean absolute profile slope value
m_q	Root-mean-square (rms) profile slope value
R	Pipe radius
R_a	Centerline average roughness height
R_{ku}	Roughness kurtosis
R_q	Root-mean-square (rms) roughness height
R_{sk}	Roughness skewness
$\mathrm{R_T}$	Turbulence Reynolds number, $k^2/(v\tilde{\varepsilon})$
Re	Pipe Reynolds number
$\mathrm{Re_d}$	Roughness Reynolds number, $UD(y)/v$
U, V	Streamwise and cross-stream velocities
U_τ	Friction velocity, $(\tau_w/\rho)^{1/2}$
x, y, z	Displacements in streamwise, cross-stream, and spanwise directions
y^+	Nondimensional distance from wall, yU_τ/v

Greek symbols

α	Topography variable (see Figures 12 and 13)
β	Nondimensional melt-down height
β_x, β_y	Ratio of area available to flow in x and y directions
γ	Topography variable (see Figures 12 and 13)
δ	Boundary-layer thickness
δ^*	Boundary-layer displacement thickness, $\int_{y=0}^{\infty} \beta_x \frac{\rho}{\rho_\infty}\left(1-\frac{U}{U_\infty}\right) dy$
ε	Topography variable (see Figure 12)
$\tilde{\varepsilon}$	"Isotropic" dissipation of turbulent energy
θ	Boundary-layer momentum thickness, $\int_{y=0}^{\infty} \beta_y \frac{\rho}{\rho_\infty}\frac{U}{U_\infty}\left(1-\frac{U}{U_\infty}\right) dy$
μ	Dynamic viscosity of fluid
v	Kinematic viscosity of fluid
ρ	Density of fluid
ϕ_a	Arithmetic mean absolute angle value
ϕ_q	Root-mean-square (rms) angle value

Subscripts

e	Free-stream conditions
H	Based on roughness peak
t	Turbulent flow
w	At wall

cone and spherical segment). A third model requires the ordinate probability distribution to generate average roughness diameters at any given height. The proposed procedures best describe the *actual* roughness topography when the roughness being modeled is dominated by a relatively narrow band of roughness sizes. Another formal restriction is that the coefficients of drag experienced by the roughness are in the postbreak-point regime (i.e., invariant with respect to Reynolds number). Otherwise, an average of the *product* of roughness diameters and coefficients of drag must be found, as suggested by Taylor *et al.*[17,19] The majority of experimental test cases investigated here satisfy these two restrictions.

Of course, the topographic modeling procedure does depend on the accuracy of the measurements of the roughness statistics, and these are by no means easy to obtain with sufficient confidence. Of particular concern may be the finite diameter of the profilometer stylus and the dependence of such statistics on the sampling length. In addition, the underlying assumption made here of spatially isotropic roughness may be questionable in certain cases. However, the results presented represent a few tentative steps to place stochastic roughness characterization on a sound mathematical basis. This is a necessary prerequisite for the application and further development of the fluid mechanics models of boundary-layer flows over stochastically rough surfaces.

Transport models

Transport equations for turbulent kinetic energy, k, and "isotropic" dissipation rate, $\tilde{\varepsilon}$, for boundary-layer flow over rough surfaces have been derived by Tarada.[21] The primary assumptions made in developing them are the same as those invoked by Taylor *et al.* and Finson *et al.* in writing their rough-flow transport equations, namely, that

- the flow is free of significant recirculation and hence can be described by a set of parabolic equations in space;
- the spatial effects of roughness can be represented by geometric "blockage factors" (which are easily calculable for the special case of roughness elements of circular cross section);
- the form drag and vortex shedding effects of roughness can be represented by sink and source terms in the momentum and turbulence equations, respectively.

The result of applying these assumptions to the transport equations of rough flow is the following set of boundary-layer equations.

- *Continuity:*

$$\frac{\partial}{\partial x}(\rho\beta_x U)+\frac{\partial}{\partial y}(\rho\beta_y V)=0$$

- *Momentum:*

$$\beta_x\rho U\frac{\partial U}{\partial x}+\beta_y\rho V\frac{\partial U}{\partial y}=-\beta_x\frac{\partial P}{\partial x}+\frac{\partial}{\partial y}\left[\beta_y(\mu+\mu_t)\frac{\partial U}{\partial y}\right]-\frac{1}{2}\frac{\rho C_D U^2 D(y)}{L_x L_z}$$

- *Kinetic energy of turbulence:*

$$\beta_x\rho U\frac{\partial k}{\partial x}+\beta_y\rho V\frac{\partial k}{\partial y}=\frac{\partial}{\partial y}\left[\beta_y\left(\mu+\frac{\mu_t}{\sigma_k}\right)\frac{\partial k}{\partial y}\right]+\beta_y\mu_t\left(\frac{\partial U}{\partial y}\right)^2-\rho\beta_x\tilde{\varepsilon}+\frac{\rho C_k U^3 D(y)}{L_x L_z}-2\mu\beta_x\left(\frac{\partial k^{1/2}}{\partial y}\right)^2$$

- *"Isotropic" dissipation rate:*

$$\beta_x\rho U\frac{\partial\tilde{\varepsilon}}{\partial x}+\beta_y\rho V\frac{\partial\tilde{\varepsilon}}{\partial y}=\frac{\partial}{\partial y}\left[\beta_y\left(\mu+\frac{\mu_t}{\sigma_\varepsilon}\right)\frac{\partial\tilde{\varepsilon}}{\partial y}\right]+\frac{\tilde{\varepsilon}}{k}\left[\beta_y C_{\varepsilon 1}\mu_t\left(\frac{\partial U}{\partial y}\right)^2-\rho\beta_x C_{\varepsilon 2}\tilde{\varepsilon}+C_{\varepsilon 3}\frac{\rho C_k U^3 D(y)}{L_x L_z}\right]+2\rho\nu\nu_t\left[\frac{\partial}{\partial y}\left(\beta_y\frac{\partial U}{\partial y}\right)\right]^2-2\mu\beta_x\left(\frac{\partial\tilde{\varepsilon}^{1/2}}{\partial y}\right)^2$$

where

β_x, β_y = fraction of area available to the flow;
$\beta_x=\beta_y = 1-\pi D^2(y)/(4L_xL_z)$ for flat plate and channel flow;
$\beta_x=\beta_y = 1-y/R-\pi D^2(y)/(4L_xL_z)$ for pipe flow;
C_D = coefficient of drag due to roughness;
$(C_k, C_{\varepsilon 3})=(6.0\times 10^{-4}, 0)$;

and

μ_t = turbulent viscosity
$=\rho C_\mu f_\mu k^2/\tilde{\varepsilon}$.

Chien's[22] recommendations that $f_\mu=1-\exp(-0.0115y^+)$ and C_μ, $C_{\varepsilon 1}$, $C_{\varepsilon 20}$, σ_ε, and $\sigma_k=0.09$, 1.35, 1.8, 1.3, and 1.0, with $C_{\varepsilon 2}=C_{\varepsilon 20}\{1-0.22\exp[-(R_T/6)^2]\}$, respectively, were used in this investigation.

In addition, the skin friction coefficient for rough boundary-layer flow is given by the sum of the wall skin friction and roughness drag contributions:

$$\frac{C_f}{2}=\frac{[\beta_x\mu\,\partial U/\partial y]_{y=0}+\int_{y=0}^{\infty}\frac{1}{2}\rho C_D U^2 D(y)/(L_xL_z)\,dy}{\rho_e U_e^2}$$

The boundary conditions to the flow transport equations are given by

$$U=V=k=\tilde{\varepsilon}=0 \qquad (y=0)$$

$$\partial U/\partial y=\partial k/\partial y=\partial\tilde{\varepsilon}/\partial y=0 \qquad (y\to\infty \text{ or } y=R)$$

Solution of the governing equations

For the solution of boundary layers developing over flat plates, the preceding equations were transformed by means of a compressible Falkner–Skan transformation to ensure economy of computation. Duct and pipe flows were solved by a primitive ordinate approach. The Keller box method (as utilized by Cebeci and Smith[23]) was used to develop the finite-difference equations. The pressure fields in duct and pipe flows were calculated by solving a set of variational equations that ensured the continuity of the flow. A geometrically expanding grid was used in the cross-stream direction, with progression factors of about 1.06 for flat plates and 1.12 for ducts and channels. Extensive grid independence tests were carried out to ensure that reported predictions did not deviate more than 1% from grid-independent solutions; generally about 100 points were used across the boundary layer, with about half of them within the roughness zone.

In addition to the calculations of rough-wall flow reported here, the turbulence model described previously has been successfully tested by Tarada[21] for its very-near-wall predictions of smooth flow and also for its performance in boundary-layer flows with streamwise curvature (where an algebraic stress model was utilized).

Drag coefficient model

The experimental database pertaining to *deterministic* roughness chosen for this investigation includes the data of Schlichting,[2]

Table 2 Summary of drag coefficients of experimental data sets

	Scaggs *et al.*	Chen	Zukauskas	Schlichting	Marshall	Gaudet
Postbreak-point	✓	✓	✓	✓	✓	✓
Prebreak-point	✓	✓	✓			
Isolated	✓	✓	✓	✓	✓	✓
Wake interference	✓	✓		✓	✓	
Skimming				✓		

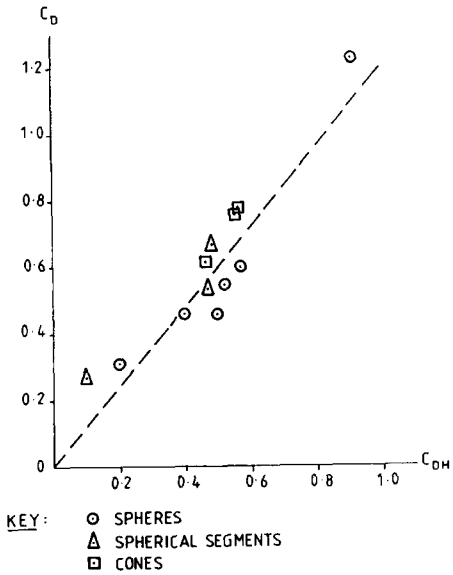

Figure 1 Postdicted versus quoted C_D valves (uncorrected Schlichting data)

Marshall,[24] Chen,[25] Gaudet,[26] Zukauskas,[27] and Scaggs *et al.*,[28] an overview of which is presented in Table 2. Experimental measurements of *local* roughness drag coefficients (i.e., based on local velocity) were not reported for the majority of test cases calculated here. Therefore an "inverse" procedure was adopted in the quest for correlations of roughness drag coefficient, C_D, indicated by the experimental data. Test functions for C_D were tried, and the differences between the resulting predictions of skin friction and the experimental data were translated into corrected values for C_D, assuming no change in local velocities. One or two iterations were sufficient for this procedure to converge. The resulting "pseudo-experimental" values of drag coefficient were then correlated into a functional form. To provide a simple check on the postdiction procedure, Schlichting's quoted coefficients of drag based on the velocity at the roughness peaks (C_{DH}) were compared to the calculated values of C_D (see Figure 1). The values of C_D were approximately 20% higher than C_{DH}, which is understandable as C_D relates to the (smaller) velocities *beneath* the roughness peaks.

To avoid the danger of arriving at postdictions rather than predictions of the experimental data sets, as large a number of independent test cases as possible were considered. One set (Chen's) was precluded from the "inverse" procedure to provide an indication of the predictive capability of the model.

The model for C_D proposed here is

$$C_D = C_D\left(\mathrm{Re_d}, \frac{1}{L_c^{1/2}}, \frac{H}{\bar{D}}, \beta_x\right)$$

The influence of each of the four arguments in C_D will now be investigated in turn.

Table 3 Scaggs *et al.*'s roughness configurations

Surface	D_0 (mm)	L (mm)	H (mm)	Projected H (mm)	$1/L_c^{1/2}$	$H/\bar{D}$
Large hemispheres						
A-1	2.55	5.10	1.25	—	3.23	0.627
A-2	2.55	10.20	1.25	—	6.46	0.627
A-3	2.55	20.25	1.15	—	13.95	0.590
Cones						
A-4	2.50	5.05	1.30	1.52	4.28	1.22
A-5	2.55	10.10	1.30	1.52	8.48	1.19
A-6	2.50	20.25	1.25	1.52	17.86	1.22
Small hemispheres						
B-1	1.25	2.50	0.65	—	3.11	0.655
B-2	1.25	5.05	0.60	—	6.62	0.618
B-3	1.30	10.10	0.55	—	13.75	0.561

Variation of C_D with respect to $\mathrm{Re_d}$

Scaggs *et al.*[28] reported the pressure drops across a rough pipe approximately 51.5 mm in diameter over the widest range of Reynolds number of all the test cases investigated here ($\mathrm{Re} = 10^4$ to 6×10^5). Three types of roughness elements (small hemispheres, large hemispheres, and cones) in three levels of packing density were investigated (see Table 3). Figure 2 shows the values of C_D extracted from the experimental friction factors using the procedure already described, correlated as functions of the *maximum* $\mathrm{Re_d}$ values within the roughness zone $y < H$. The results indicate that beyond a break-point value of $\mathrm{Re_d}$, denoted $\mathrm{Re_{dc}}$, the drag coefficients are broadly constant. Figure 3 shows the variation of $\mathrm{Re_{dc}}$ with $1/L_c^{1/2}$, from which it may be estimated that:

$$\mathrm{Re_{dc}} = \frac{4.35 \times 10^2}{L_c^{1/2}} \quad \text{for} \quad \frac{1}{L_c^{1/2}} < 11.5,$$

and

$$\mathrm{Re_{dc}} = 5.0 \times 10^3 \quad \text{for} \quad \frac{1}{L_c^{1/2}} \geq 11.5.$$

Regression analysis indicates that for the range $150 < \mathrm{Re_d} < \mathrm{Re_{dc}}$, C_D varies as $\mathrm{Re_d}^{-0.289}$ and that below $\mathrm{Re_d} = 150$, C_D varies as $\mathrm{Re_d}^{-1.874}$. However, as the correlations of C_D are meant to be used as functions of *local*, not *maximum* $\mathrm{Re_d}$ values within the roughness zone, no exponent of $\mathrm{Re_d}$ less than -1 can be entertained, because infinite roughness momentum sink terms would result in regions where $D(y) \to 0$. Therefore a uniform prebreak-point variation of C_D as $\mathrm{Re_d}^{-0.289}$ was assumed. This made little difference to the computations, because at very low Reynolds numbers the proportion of the total skin friction attributable to roughness form drag is small. Despite this small anomaly, which is due to the neglect of the skin friction drag on the roughness elements themselves (see Topographic models section), the overall assumption in interpreting the correlations of C_D versus maximum $\mathrm{Re_d}$ as being applicable to local $\mathrm{Re_d}$'s

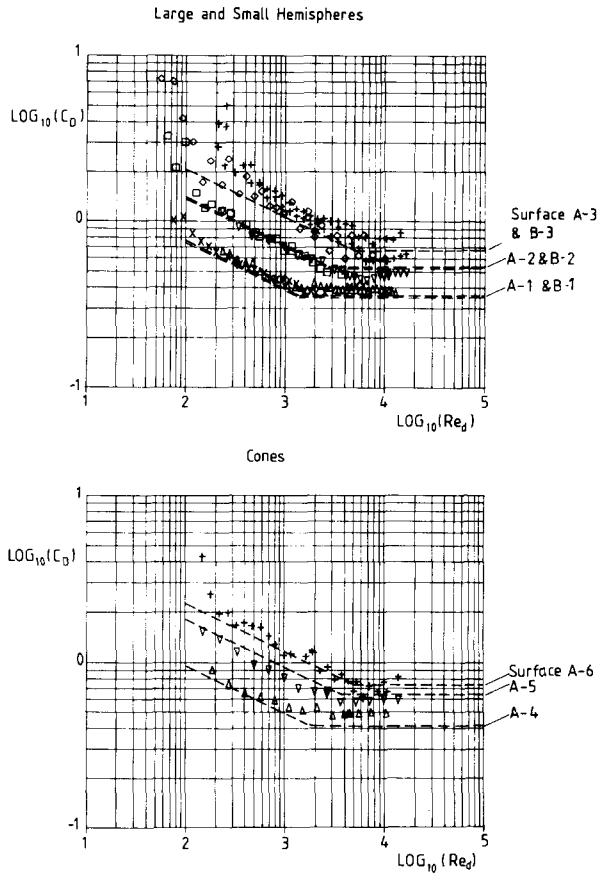

Figure 2 Postdictions and correlations of Scaggs *et al.*'s roughness drag coefficients, large hemispheres and cones (current correlation ----)

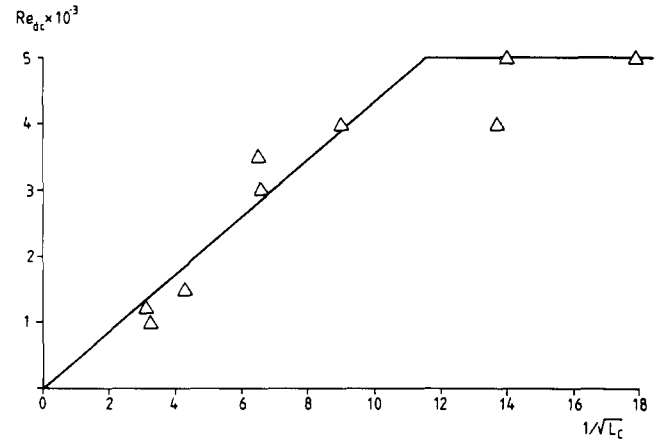

Figure 3 Variation of Re_{dc} with respect to $1/L_c^{1/2}$ (based on postdictions of Scaggs *et al.*'s data)

as well, implying that the regions of maximum drag production lie close to where the maximum values of Re_d are generated, was well vindicated by subsequent computations.

Variation of C_D with respect to $1/L_c^{1/2}$

Morris[29] identified three roughness flow regimes influenced by packing density: *isolated* roughness flow, where roughness elements are far enough apart to escape any wakes shed by upstream elements, and drag coefficients are therefore independent of packing density in this regime; *wake interference* flow, where wakes do impinge on downstream elements and where drag coefficients collapse significantly from their isolated flow values; and quasi-smooth, or *skimming* flow, where the packing density is so great that effectively a new, smooth surface is generated at the top of the roughness elements. Figure 4 shows the drag coefficient postdictions relating to Marshall's measurements of the (postbreak-point) drag on a plate roughened with cylinders of various aspect ratios and hemispheres. These postdictions show clearly the isolated flow regime, where C_D is dependent only on the aspect ratio $H/\bar{D}$, and the wake interference flow, where C_D is dependent only on $1/L_c^{1/2}$. A small "overshoot" is observed in the transition region between the two regimes.

Schlichting's results (as corrected by Coleman *et al.*[30]) for the range of roughness levels summarized in Table 4, all of which lie in the postbreak-point Reynolds number regime, were also analyzed for trends with respect to packing density. Figure 5 shows the variation of local C_D with respect to $1/L_c^{1/2}$ for Schlichting's and Scaggs *et al.*'s data, from which the interference-regime correlation

$$C_D = 0.182 + \frac{0.0542}{L_c^{1/2}}$$

can be extracted. Marshall's interference regime coefficients of drag have not been included in the correlation. The reason is that the reported variation of C_D with respect to streamwise distance in Marshall's interference-regime test cases made it difficult to obtain postdictions with sufficient confidence.

Variation of C_D with respect to $H/\bar{D}$

It was hypothesized that the variation of C_D with respect to aspect ratio, $H/\bar{D}$, for postbreak-point, isolated roughness elements may follow an exponential-type law of the form:

$$C_D = C_{D\infty} - (C_{D\infty} - C_{D,\min}) \exp\left[-\alpha (H/\bar{D})^n\right]$$

In this equation, $C_{D\infty}$ is the postbreak-point drag coefficient for an isolated circular roughness element of infinite aspect ratio, with a value approximately equal to 1.1 from Zukauskas's measurements (see Figure 6). $C_{D,\min}$ is the minimum drag coefficient of an isolated roughness element in the postbreak-point Reynolds number regime; its value was found to be approximately 0.4 by computer optimization of all the experimental data reviewed.

Apart from these sources of data, the data of Gaudet[26] was particularly useful in fixing the parameters of the model; the drag coefficients reported by Gaudet for isolated cylinders of various aspect ratios (for a free-stream Mach number of 0.2)

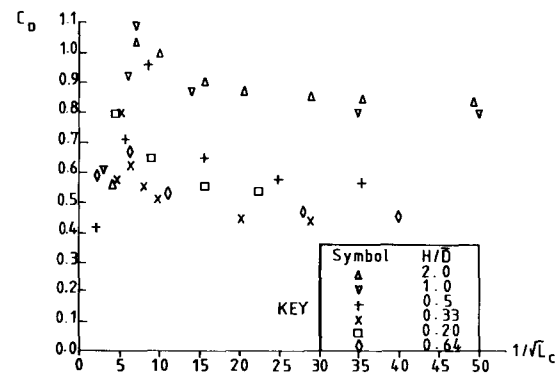

Figure 4 Postdictions of Marshall's C_D values

Table 4 Schlichting's roughness configurations

Plate No.	D_{max} (cm)	L_x (cm)	L_z (cm)	H (cm)	Projected H (cm)	$1/L_c^{1/2}$	$H/\bar{D}$
			Spheres				
XII	0.41	4	4	0.41	—	11.29	1.27
III	0.41	2	2	0.41	—	5.64	1.27
I	0.41	1	1	0.41	—	2.82	1.27
II	0.41	0.6	0.6	0.41	—	1.69	1.27
V	0.41	0.41	0.36	0.41	—	1.05	1.27
VI	0.21	1	1	0.21	—	5.64	1.27
IV	0.21	0.5	0.5	0.21	—	2.82	1.27
			Spherical segments				
XIII	0.8	4	4	0.26	—	10.72	0.45
XIV	0.8	3	3	0.26	—	8.03	0.45
XV	0.8	2	2	0.26	—	5.36	0.45
XIX	0.8	0.8	0.69	0.26	—	2.00	0.45
			Truncated cones				
XXIII	0.8	4	4	0.375	0.425	9.71	0.84
XXIV	0.8	3	3	0.375	0.425	7.27	0.84
XXV	0.8	2	2	0.375	0.425	4.85	0.84

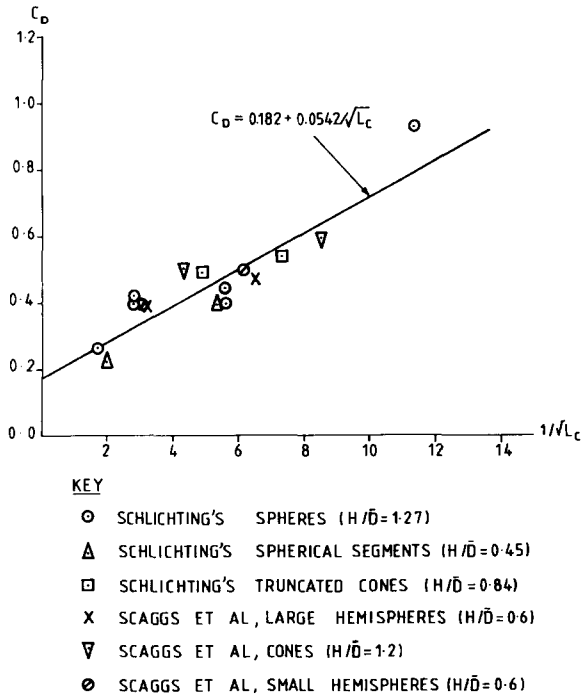

Figure 5 Postbreak-point drag coefficients in the wake interference regime (Schlichting and Scaggs *et al.*'s data)

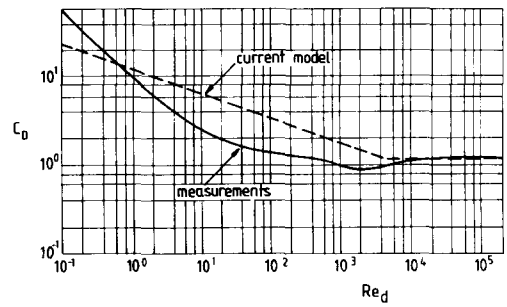

Figure 6 Variation of C_D with respect to Re_d for cylinders of infinite aspect ratio (measurements of Zukauskas[27])

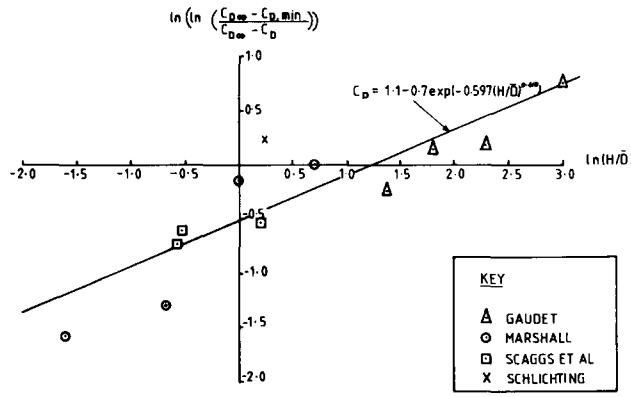

Figure 7 Variation of C_D with respect to $H/\bar{D}$ in the isolated postbreak-point regime

were converted to their equivalent local velocity base by use of the velocity profile information quoted by Winter and Gaudet.[31] Figure 7 shows the correlation of Marshall's, Schlichting's, Gaudet's, and Scaggs *et al.*'s postbreak-point data with respect to $H/\bar{D}$ in the exponential form proposed. Not every point could be included, because the logarithmic function behaved singularly for drag coefficients close to or less than $C_{D,min}$. However, the preponderance of data points indicated regression values of α and n equal to 0.597 and 0.419, respectively.

Variation of C_D with respect to β_x

For skimming flow, where the roughness packing densities are very high (i.e., $1/L_c^{1/2}$ is low), the dimensions of the gaps between the roughness elements may be so small that the gap Reynolds number may be in the laminar regime. By analogy with the hydraulic diameter of laminar channel flow, we may estimate that the laminar value of C_D for rough flow is given by

$$C_D = \frac{16}{\beta_x \mathrm{Re}_d}$$

This value is negligibly small for typical Re_d values of 10^4 or so, but is significant when β_x [taken here to mean $1 - \pi D^2(y)/(4L_xL_z)$

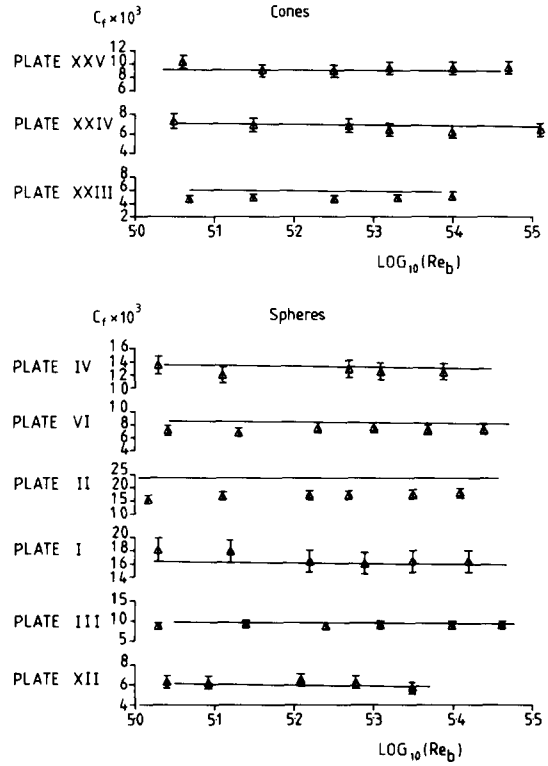

Figure 8(a) Predictions of Schlichting's rough-wall skin-friction data (cones and hemispheres)

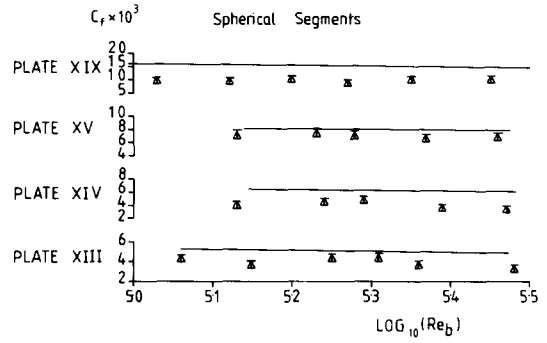

Figure 8(b) Predictions of Schlichting's rough-wall skin-friction data (spherical segments)

for both flat-plate and tube flow] tends toward zero. This laminar value of C_D was added to the estimate given by the previous correlations so that the correct trend is reproduced when $\beta_x \to 0$. No such correction was required for cases where $\beta_x \to 1$.

Overall C_D model

In summary, we may write the overall C_D model as

$$\mathrm{Re}_{dc} = \min\left[\frac{4.35\times 10^2}{L_c^{1/2}},\ 5\times 10^3\right]$$

$$C_{DP} = \min\left\{0.182 + \frac{0.0542}{L_c^{1/2}},\ 1.1 - 0.7\exp\left[-0.597\left(\frac{H}{\bar{D}}\right)^{0.419}\right]\right\}$$

$$C_D = \max\left[C_{DP},\ C_{DP}\left(\frac{\mathrm{Re}_d}{\mathrm{Re}_{dc}}\right)^{-0.289}\right] + \frac{16}{\mathrm{Re}_d}(\beta_x^{-1} - 1)$$

Predictions of rough-wall flow

Using this C_D model in conjunction with the k–ε model described earlier, we arrive at predictions for the data of Schlichting, Scaggs *et al.*, and Chen, presented in Figures 8–11, respectively. In view of the uncertainties surrounding Coleman *et al.*'s corrections of Schlichting's data, (arbitrary) error bands of $\pm 10\%$ have been assigned to the corrected skin friction values. Figure 8 shows that the majority of Schlichting's data is well predicted by the current model, except for the highly packed spherical (plate II) and spherical segment (plate XIX) test cases. This result is due to the particular C_D versus $1/L_c^{1/2}$ correlation adopted for the wake interference regime, which of course is a compromise between Schlichting's and Scaggs *et al.*'s data. No predictions could be obtained for Schlichting's test case of spheres in the densest possible packing (plate V), because problems with numerical convergence were experienced for the flow below the midplane of the roughness elements. The problems with convergence stemmed from the collapse of the predicted local flow velocities. In reality, the flow field below the midplane of the spheres is of a highly recirculatory nature and therefore cannot be handled by a parabolic routine such as the one employed here. The problems associated with predicting Schlichting's plate V test case were typical of those encountered when calculating rough boundary-layer flow in the skimming flow regime.

Figure 9 shows the excellent predictions obtained for Scaggs *et al.*'s data, which do not require further comment. Figure 10 shows the predicted pipe friction factors and ratio of smooth to total skin friction, τ_s/τ_0, for Chen's data, a summary of whose roughness configurations appears in Table 5. As explained

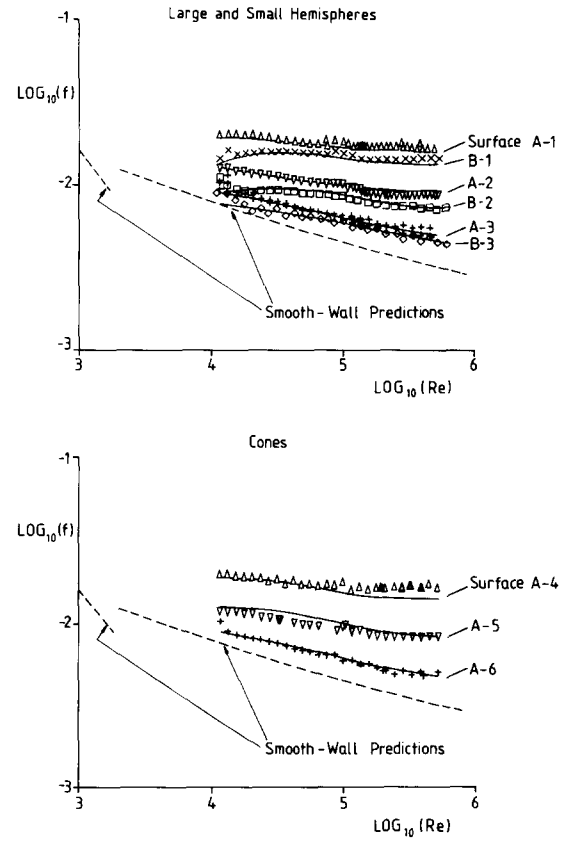

Figure 9 Predictions of Scaggs *et al.*'s rough-pipe friction factors (large hemispheres and cones)

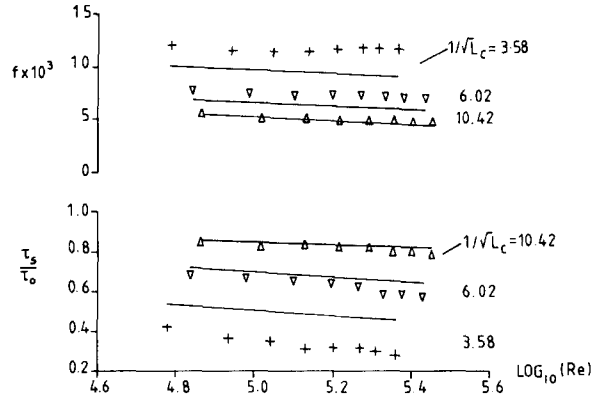

Figure 10 Predictions of Chen's friction factor and shear stress partition data

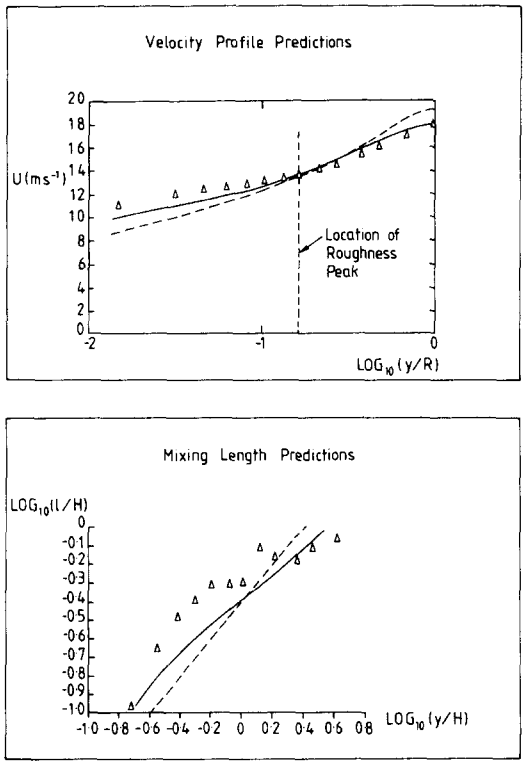

Figure 11 Predictions of Chen's velocity and mixing-length profiles, using k–ε and mixing-length models ($\mathrm{Re}=1.86\times10^5$, $1/L_c^{1/2}=3.58$, ---- mixing length; —— k–ε predictions)

previously, these are genuine predictions, because Chen's database was not employed in setting up the C_D model. The predictions are generally satisfactory, except for those relating to the densest packing. Chen measured both the mean velocity profile and turbulent shear stress ($-\overline{\rho u'v'}$) *between* the roughness elements, so we may make a direct comparison between the turbulent mixing-length predicted by the current model and that given by a "standard" van Driest mixing-length model (as utilized in Reference 17),

$$l=\min\{0.40y(1-\exp[-y^+/26]),\ 0.09\delta\}$$

Figure 11 shows predicted and experimental local mixing length to roughness height ratio, l/H, and velocity profiles for the largest size of roughness elements investigated by Chen. Mixing lengths were recomputed from Chen's raw data, as the mixing lengths he reported were based on an *average* velocity slope within the roughness zone, rather than a *local* slope. Figure 11 shows that the k–$\tilde{\varepsilon}$ model goes part way toward predicting both the mixing-length enhancement for $y/H<1$ and the mixing-length suppression for $y/H>1$. It therefore provides better predictions of the measured velocity profiles than does the Prandtl mixing-length model (the suppression effect is due to the large velocity gradients immediately above the roughness elements). Although Taylor *et al.* managed to obtain good predictions for Chen's friction factors using relatively large C_D values (see Table 1), the simple mixing-length model they used is responsible for significant underpredictions of velocity within the roughness zone. The current model's ability to capture the mixing-length enhancement effect is due to the extra production of turbulent kinetic energy within the roughness zone caused by the interaction between eddy viscosity and the roughness-distorted velocity profile.

Topographic models of stochastic roughness

In order to apply the turbulence and drag coefficient model to the prediction of flows over *stochastic* roughness, it is necessary to characterize geometrically the roughness. We do so by means of three topographical models.

Topographic model I (truncated cones)

A sketch of the proposed roughness topographic model is presented in Figure 12. The model topography consists of upright and inverted cones, both having spacings of L_x and L_z in the x and z directions, respectively.

The procedure involves equating the ordinate moment statistics (up to fourth order), plus one profile slope parameter, of the modeled topography to the corresponding measured values pertaining to the real stochastically rough surface, in order to fix the dimensions of the model surface. Analysis of the truncated cone topography yields Equations A1–A3 in the Appendix.

Table 5 Chen's roughness configurations (hemispheres)

D_{max} (mm)	L_x (m)	L_z (m)	$1/L_c^{1/2}$	$H/\bar{D}$
10.97	0.10	0.20	10.42	0.64
19.05	0.10	0.20	6.02	0.64
31.75	0.10	0.20	3.58	0.64

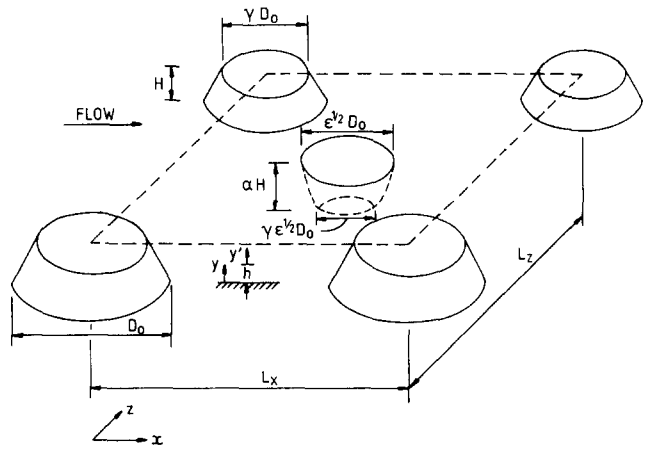

Figure 12 Topographic model I (truncated cone model)

To arrive at these equations, we assumed that $\beta \geq 0$. That is, the melt-down location lies above the "wall" location, which is consistent with the underlying assumption that the roughness is dominated by peaks, not troughs.

The relationships between the nondimensional ordinate moment functions $f_n(\alpha, \beta, \gamma, \varepsilon)$ and the common engineering ordinate moments (as defined in BS 1134 and ISO 468, for example) are given by

R_a = centerline roughness height
$= Hf_1$

R_q = root-mean-square (rms) roughness height
$= Hf_2^{1/2}$

R_{sk} = roughness skewness
$= f_3/f_2^{3/2}$

R_{ku} = roughness kurtosis
$= f_4/f_2^2$.

The profile skewness is a measure of the asymmetry of the roughness profile (it is positive when peaks are more prominent than troughs). The profile kurtosis is a measure of the "spikedness" of a surface; $R_{ku} > 3$ indicates sharp peaks and troughs. For roughness with a Gaussian distribution of ordinates,

$$R_q/R_a = (\pi/2)^{1/2}, \qquad R_{sk} = 0 \quad \text{and} \quad R_{ku} = 3.$$

Besides the values of R_a, R_q, R_{sk}, and R_{ku}, we also require an average angle or slope parameter to fix the dimensions of the model surface. Four options are listed in Equations A4–A7 in the Appendix, of which only *one* is required for a given case. However, even with all this information we are still left with six equations and seven unknowns ($\alpha, \beta, \gamma, \varepsilon, H, L, D_0$). Hence, ideally, a further piece of information—for example, the fifth-order ordinate moment statistic—should be included to provide a closed set. However, few experimental ordinate data sets are of sufficient quality to enable the evaluation of such a statistic, so a compromise is proposed here. It involves setting the value of α as close to unity as the feasible solution space allows, unity being the Gaussian distribution value. This practice seemed justified by the good predictions obtained for a wide range of data.

The topographic modeling procedure for model I involves, in summary, the following steps.

(1) Measurement of R_a, R_q, R_{sk}, and R_{ku} and m_a, m_q, ϕ_a, or ϕ_q of stochastic roughness.
(2) Solution of the equations

$$\frac{R_q}{R_a} - \frac{f_2^{1/2}}{f_1} = 0$$

$$R_{sk} - \frac{f_3}{f_2^{3/2}} = 0$$

$$R_{ku} - \frac{f_4}{f_2^2} = 0$$

for β, γ, and ε for a near-unity value of α.
(3) Evaluation of H from

$$H = \frac{R_a}{f_1} = \frac{R_q}{f_2^{1/2}}$$

(4) Evaluation of D_0 from *one* of Equations A4–A7 (corresponding to experimental data of profile slope or angle).
(5) Evaluation of $L = (L_x L_z)^{1/2}$ from Equation A1.

Limiting inequalities

Several checks can be applied to this procedure to ensure physical realizability. First, by considering the condition of maximum packing density (for $0 \leq \gamma \leq 1$), which, in the absence of troughs, implies that

$$\frac{D_0^2}{L_x L_z} \leq \frac{2}{3^{1/2}}$$

the sufficient but not necessary condition that

$$\beta \leq \frac{\pi}{6(3^{1/2})} \frac{(1+\gamma+\gamma^2)(1-\alpha\varepsilon)}{(1+\varepsilon)}$$

may be inferred.

A necessary but not sufficient condition may be inferred from the area limitation that

$$(1+\varepsilon)\frac{\pi}{4} D_0^2 < L_x L_z$$

which implies that

$$\beta < \frac{1}{3} \frac{(1+\gamma+\gamma^2)(1-\alpha\varepsilon)}{(1+\varepsilon)}$$

Finally, the Cauchy–Schwarz inequality

$$\int_a^b fg\, dx \leq \left(\int_a^b f^2\, dx \int_a^b g^2\, dx \right)^{1/2}$$

for any functions f and g may be invoked to show that

$$R_a \leq R_q \quad \text{and} \quad R_{sk} \leq R_{ku}^{1/2}$$

These two inequalities serve as useful checks on the experimental values of the statistical quantities.

Topographic inputs into boundary-layer prediction routine

With regard to the boundary-layer calculations, the location of the "wall" was assumed to be at the base of the truncated cones (i.e., at $y=0$ or $y' = -h$), as no significant flow was assumed to occur within the troughs.

The variation of roughness element diameter with distance from the wall, described by

$$D(y) = D_0[1-(1-\gamma)y/H] \quad \text{for } 0 \leq y \leq H$$

$$D(y) = 0 \quad \text{for } y > H$$

as well as the spacing parameter L constituted the topographic information required by the boundary-layer prediction routine.

Topographic model II (spherical segments)

A sketch of this proposed roughness topographic model is shown in Figure 13. The model consists of upright and inverted spherical segments, both having spacings of L_x and L_z in the x and z directions, respectively.

The modeling procedure adopted in this model is similar to that of model I (truncated cone model). Performing the requisite integrations yields equations A8–A14 in the Appendix.

The topographic modeling procedure for model II, in summary, involves the following steps.

(1) Measurement of R_a, R_q, and R_{sk} and m_a, m_q, ϕ_a, or ϕ_q of stochastic roughness.
(2) Solution of the equations

$$\frac{R_q}{R_a} - \frac{f_2^{1/2}}{f_1} = 0$$

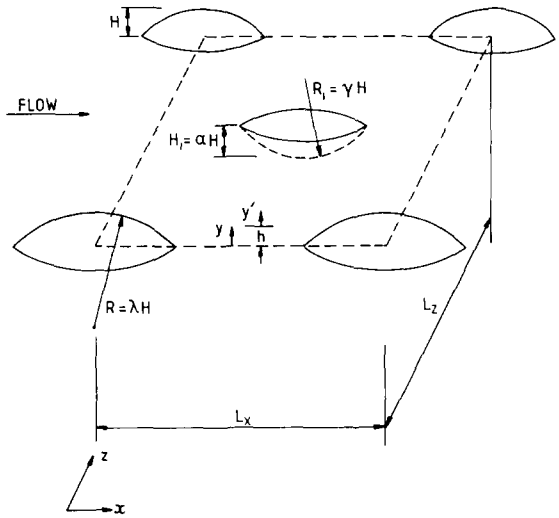

Figure 13 Topographic model II (spherical segment model)

$$R_{sk} - \frac{f_3}{f_2^{3/2}} = 0$$

$$R_{ku} - \frac{f_4}{f_2^2} = 0$$

and *one* of Equations A11–A14 to solve for α, β, γ, and λ.

(3) Evaluation of H from

$$H = \frac{R_a}{f_1} = \frac{R_q}{f_2^{1/2}};$$

(4) Evaluation of L from Equation A8.

Limiting inequalities

As for model I, we may write a sufficient but not necessary packing density condition that

$$\beta \le \frac{\pi}{2(3^{1/2})} \frac{\lambda - 1/3 - \alpha^3(\gamma - \alpha/3)}{2\lambda - 1 + 2\gamma\alpha - \alpha^2}$$

and a necessary but insufficient condition that

$$\beta \le \frac{\lambda - 1/3 - \alpha^3(\gamma - \alpha/3)}{2\lambda - 1 + 2\gamma\alpha - \alpha^2}$$

Topographic inputs into boundary-layer prediction routine

The topographic inputs consist of the variation of roughness element diameter with distance from the wall, described by

$$D(y) = 2H[\lambda^2 - (y/H + \lambda - 1)^2]^{1/2} \qquad \text{for } 0 \le y \le H$$

$$D(y) = 0 \qquad \text{for } y > H$$

as well as the spacing parameter L.

Topographic model III (probability density curve)

The shape of an "average" roughness element within a stochastic roughness distribution may be found from the ordinate probability density function. As the infinitesimal probability (δP) of an ordinate y' above the mean line (melt-down location) is proportional to the infinitesimal width (δx) of that ordinate, it follows that

$$\delta P = \frac{\delta x}{L}$$

where L is the transverse distance between the top and bottom of the roughness element.

Defining the probability density function (f) as $f = dP/dy$, it follows that

$$\frac{x(y')}{L} = \int_{y=H_1}^{y'} f \, dy$$

where H_1 is the bottom limit of y.

Because the ordinates are usually normalized by a length scale H^* (typically R_a or R_q), a nondimensional probability density function $f^* = H^* f$ is obtained. The preceding equation can therefore be written in functional form as

$$\frac{x(y'/H^*)}{L} = \int_{z'=H_1/H^*}^{y'/H^*} f^* \, dz'$$

where

$$z' = \frac{y}{H^*}$$

This equation enables the shape of an "average" roughness element to be generated from measurements of the ordinate probability density function.

The determination of the length scale L involves equating a slope or angle parameter calculated from the curve implied by the above equation to that given by the probability density functions of slopes or angles. As

$$\text{slope} = d(y/H^*)/d(x/H^*) = (f^*)^{-1}(L/H^*)^{-1}$$

we can calculate

$$\frac{L}{H^*} = \frac{\int_{u=0}^{1} (f^*)^{-1} \, du}{m_a}$$

or

$$\frac{L}{H^*} = \frac{[\int_{u=0}^{1} (f^*)^{-2} \, du]^{1/2}}{m_q}$$

or solve for (L/H^*) from

$$\phi_a - \int_{u=0}^{1} \arctan\left[\frac{1}{f^*(L/H^*)}\right] du = 0$$

or

$$\phi_q - \left\{\int_{u=0}^{1} \left[\arctan\left(\frac{1}{f^*(L/H^*)}\right)\right]^2 du\right\}^{1/2} = 0$$

where $u = x/L$.

Having estimated L, we may find $D(y)$ from

$$D(y) = L\left\{\frac{4}{\pi}\left[1 - \frac{x(y)}{L}\right]\right\}^{1/2}$$

which is a consequence of equating the (three-dimensional) free space available in the topographical model to that implied by the probability density curve.

The location of the boundary-layer origin (the "wall") in this model may be heuristically defined as the value of y' corresponding to the peak in the ordinate probability density function, i.e., where the largest concentration of flat surface occurs. This location does not, in general, coincide with the melt-down location defined by $y' = 0$.

Figure 14 shows a comparison between the side views of roughness elements generated by models I and III for a typical test case.

Choice of slope and angle parameters

In the three topographic models presented, we are faced with a choice in selecting one of four possible candidates of slope and angle parameters in order to fix the transverse length-scale

L. The question then immediately arises as to the consistency of the results when different choices are made. The probability density distributions of models I and II are only poor approximations to the real stochastic distributions. Thus the values of L calculated from absolute parameters may not be the same as those calculated from rms parameters. From computations using the roughness database reported in Reference 21, the values of L given by an m_a base were consistently closer to the wavelength parameters $\lambda_a = 2\pi R_a/m_a$ and $\lambda_q = 2\pi R_q/m_q$ ($\lambda_a = \lambda_q$ for Gaussian roughness) than those given by an m_q base using model I. The latter values were generally too high by 20–50%. Therefore all predictions using models I and II here utilize *absolute* angle and slope rather than rms parameters. None of the data sets available contained both angle and slope data, so it was not possible to ascertain any differences in L due to the choice of angle as opposed to slope parameters.

Model III (probability density curve) does not suffer from the same discrepancies, values of L calculated from absolute and rms angles being very close. This result is not surprising because of the much closer approximation to reality that this model provides.

Boundary-layer model

It is necessary here to specify the initial profiles of the velocity and turbulence variables, which influence development of the boundary-layer from laminar to turbulent flow. The initial momentum thickness was computed from Thwaites's integral equation, and the initial (laminar) velocity profile was described by a Pohlhausen fourth-degree-type equation. The initial turbulent kinetic energy profile is given by

$$k = k_\infty \left(\frac{U}{U_\infty}\right)^2$$

after Rodi and Scheuerer.[32]

The initial dissipation profile is given by

$$\tilde{\varepsilon} = \frac{k^{3/2}}{2.5y}\left[1 + (-6+3\Pi)\left(\frac{y}{\delta}\right)^2 + (8-3\Pi)\left(\frac{y}{\delta}\right)^3 + (\Pi-3)\left(\frac{y}{\delta}\right)^4\right]$$

where $\Pi = 2.5\tilde{\varepsilon}_\infty \delta / k_\infty^{3/2}$. This profile ensured a smooth transition between the inner boundary-layer "equilibrium" values of $\tilde{\varepsilon}$ (found by equating the production to dissipation of k), and the free-stream value of $\tilde{\varepsilon}$, namely $\tilde{\varepsilon}_\infty$.

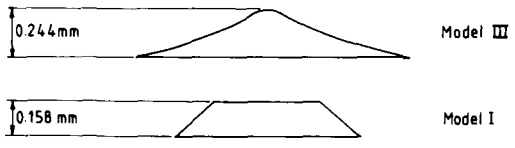

Figure 14 Comparison of side views of roughness elements generated by models I and III for Acharya *et al.*'s cast surface

The free-stream values of k and $\tilde{\varepsilon}$ were found from correlations of the decay of turbulence behind a grid. The usual form of such correlations is

$$Tu = \frac{u'}{U_\infty} = a\left(\frac{x}{b}\right)^{-n}$$

where b is the effective bar size (3.2mm for Al-Shukri's G_4^3 grid for example), and a and n are typically 1.12 and 5/7, respectively.

Assuming an isotropic free stream, we may estimate

$$k_\infty = \tfrac{3}{2} Tu^2 U_\infty^2$$

and

$$\tilde{\varepsilon}_\infty = 3\frac{n}{x} U_\infty^3 Tu^2.$$

Predictions of stochastic rough-wall data

Predictions of the data of Karlsson,[33] Al-Shukri,[34] Acharya *et al.*,[35] and Watt[36] are presented in this section. These data sets were chosen because they contain at least some of the information required to apply one or more of our topographic models. Karlsson's, Al-Shukri's and Acharya *et al.*'s databases include skin friction measurements; transition locations were measured by Al-Shukri and Watt.

Table 6 gives a summary of the statistical surface data required to implement models I and II for the test cases chosen. Al-Shukri did not measure any angle or slope parameters, so we used Tarada's[21] slope measurements of the roughness generated by aluminum oxide grade 150, which is nominally the same as Al-Shukri's K3 roughness. The same work was also utilized in setting up the parameters of Watt's unpolished thermal barrier coating (TBC) roughness; this approach can be partially supported by the fact that both Watt's and Tarada's TBC surfaces were produced by an identical process and by the same firm.

Acharya *et al.*'s published roughness statistics do not satisfy the Cauchy–Schwarz inequality. Correspondence with Professor Acharya and Dr. Bornstein indicated the existence of a bug in the latter's results processing software. The ordinate moment statistics for Acharya *et al.*'s surfaces listed in Table 6 were computed directly from the probability density values supplied by Dr. Bornstein.

Skin friction predictions

Table 7 lists the results of applying model I to the seven stochastically rough surfaces in Table 6. Figure 15 shows the skin friction predictions of Karlsson's surfaces 1 and 3, using model I. The predictions are poor in the middle of the unit Reynolds number range for surface 3, but are generally acceptable for surface 1. However, the behavior of Karlsson's surface 3 is somewhat idiosyncratic, since the fully rough skin friction co-

Table 6 Summary of roughness statistics

Surface	R_a (μm)	R_q (μm)	R_{sk}	R_k	ϕ_a (°)	ϕ_q (°)	m_a	m_q
Karlsson 1	25	31	0.5	2.4	0.021	0.028	—	—
Karlsson 3	148	183	0.1	2.7	0.13	0.22	—	—
Al-Shukri, K3	79	93	−0.24	3.20	—	—	0.40	0.66
Acharya *et al.*, cast	53	63	0.72	3.44	0.21	0.26	—	—
Acharya *et al.*, SRS1	98	117	0.57	3.29	0.098	0.13	—	—
Acharya *et al.*, SRS2	112	141	0.58	3.13	0.13	0.16	—	—
Watt, unpolished TBC	11.6	14.3	0.3	3.0	—	—	0.14	0.18

Table 7 Model I results

Surface	α	γ	H (mm)	D_0 (mm)	L (mm)	$1/L_c^{1/2}$	H/D
Karlsson 1	0.6	0.643	0.065	5.37	7.87	14.7	0.015
Karlsson 3	0.9	0.717	0.360	4.53	6.52	5.51	0.092
Al-Shukri, K3	1.2	0.691	0.183	1.04	1.32	3.28	0.207
Acharya *et al.*, cast	1.2	0.583	0.158	0.838	1.175	3.63	0.238
Acharya *et al.*, SRS1	1.2	0.709	0.272	3.458	5.139	5.73	0.092
Acharya *et al.*, SRS2	0.9	0.765	0.316	2.397	3.871	4.73	0.149
Watt, unpolished TBC	1.0	0.825	0.030	0.329	0.514	5.46	0.098

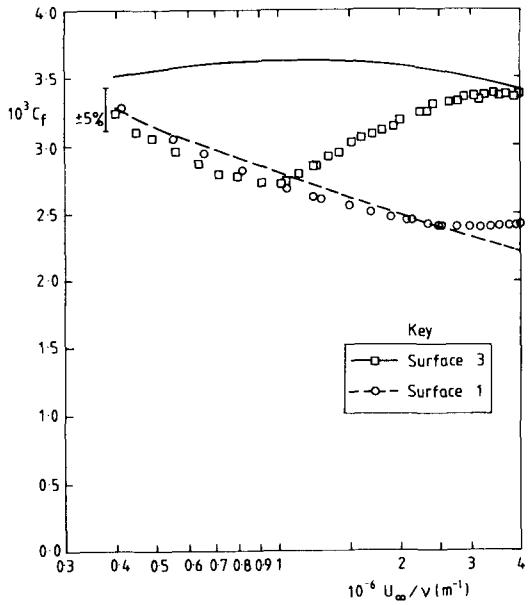

Figure 15 Predictions of Karlsson's skin-friction data

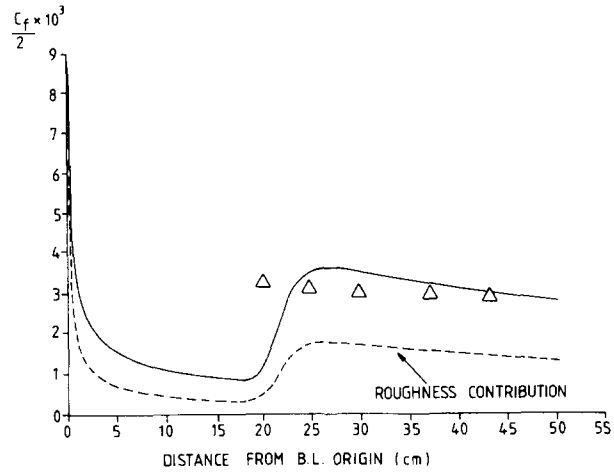

Figure 16 Predictions of Al-Shukri skin friction coefficients (U_∞ = 14 m s^{-1}; K3 roughness)

efficient asymptote is experimentally observed to be approached from *below* with increasing unit Reynolds number, contrary to what is normally observed on most stochastically rough surfaces. The correct (fully rough) skin friction asymptotic level, however, is predicted for large unit Reynolds numbers on surface 3.

Figure 16 shows the skin friction predictions of Al-Shukri's K3 roughness for a free-stream velocity of 14 m s^{-1}. The predictions are generally within the uncertainty range of the experimental data, which was arrived at by the error-prone momentum thickness differentiation method.

Application of model III to Acharya *et al.*'s data resulted in values of L equal to 1.50, 6.44, and 5.50 mm for the cast, SRS1, and SRS2 surfaces, respectively. The skin friction, shape factor and momentum thickness predictions of Acharya *et al.*'s $U_\infty = 18.8$ m s^{-1} test cases relating to surface SRS1 are shown in Figure 17. Surfaces SRS1 and SRS2 were generated from glass spheres in a substrate, so we thought that model II, the spherical segment model, might be superior to model I for these surfaces. The results of applying model II to surfaces SRS1 and SRS2 are presented in Table 8. The aspect ratio, $H/\bar{D}$, for spherical segments was calculated from

$$\frac{\bar{D}}{H} = \lambda^2 \left[\frac{\pi}{2} - \arcsin\left(\frac{\lambda - 1}{\lambda}\right) - \left(\frac{\lambda - 1}{\lambda^2}\right)(2\lambda - 1)^{1/2} \right]$$

and the value of L_c was then computed from

$$L_c = \frac{(\bar{D}/H)H^2}{L^2}$$

In practice however, there was very little difference between the predictions of models I and II. Therefore only model I predictions were plotted in Figure 17.

The main conclusion to be drawn from the predictions of Acharya *et al.*'s data is the strong correspondence between the predictions of models I, II, and III: nowhere is the difference between the models' predictions greater than 5%. Model III clearly provides the best description of the rough surface and should be used in preference to models I and II when sufficient data are available for its implementation. However, models I and II, which make use of standard profilometer data, require less overall information and hence provide an opportunity of calculating the aerodynamic characteristics of a rough wall for less cost but with accuracy nearly equal to that of model III.

Some limitations of the current models

Two limitations of the current models have already been mentioned, namely, the behavior of the models at very low roughness Reynolds numbers ($Re_d < 150$) and the difficulty of predicting flows in the skimming-flow regime. The first of these limitations, caused by neglect of the skin friction drag on the roughness elements themselves, leads to some paradoxical results in the limiting case of very small roughness height. Such roughness elements do not induce any significant *form* drag since the local velocities are very small, and therefore in such cases the current model would erroneously predict a total drag that is lower than the smooth-wall case, due to the blockage of part of the wall by the roughness elements. This limitation is not apparent in any of the predictions presented here. Further work is required to develop the rough-wall momentum equation in order to remove this limitation.

As most of the coefficients of drag used here for correlation purposes were obtained by a process of postdiction, independent measurements are needed to check the correlations, particularly in the wake interference regime. But, from the comparisons of the computed results with experimental data, the current model clearly is a powerful tool for the analysis of flow over both deterministic and stochastic roughness.

Conclusions

The low Reynolds number k–ε model, drag coefficient formulation, and topographic models presented here provide reasonable predictions for the six deterministic and four stochastic roughness boundary-layer databases investigated. Further work is required in the development of all three aspects of the models for more confident predictions to be made of rough-wall boundary-layer flows.

Acknowledgments

The author wishes to acknowledge the encouragement and support of the director and the manager of the Thermo-Fluid Mechanics Research Centre, Professor F. J. Bayley and Dr. A. B. Turner, respectively. This work was carried out under contract with the Royal Aerospace Establishment at Pyestock, England.

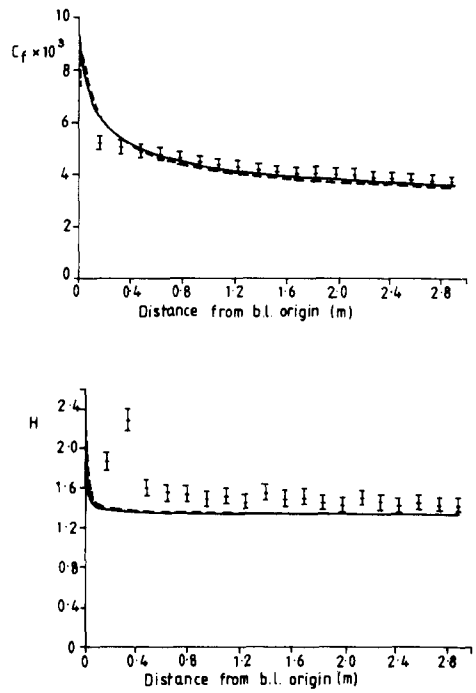

Figure 17 Predictions of C_f and H; Acharya *et al.*'s SRS1 surface data (—— model III; ---- model I predictions)

References

1 Nikuradse, J. Strömungsgesetze in rauhen Rohren. *VDI-Forschungsheft* 361, 1933; also Laws of flow in rough pipes. Aeronautical Research Committee Report BARC 986-T. 3479-F. M. 141, translated 1933
2 Schlichting, H. Experimental investigation of the problem of surface roughness. NACA translation TM-823, 1937
3 Colebrook, C. F. and White, C. M. Experiments with fluid motion in roughened pipes. *Proc. R. Soc. Lon.*, 1937, **A161**, 367–381
4 Dvorak, F. A. Calculation of turbulent boundary layers on rough surfaces in pressure gradient. *AIAA J.*, 1969, **7**(9), 1752–1759
5 Dirling, R. B. A method for computing roughwall heat transfer on reentry nosetips. AIAA 8th Thermophysics Conference, 1973, Paper 73-763
6 Christoph, G. H. Roughness effects in Head's integral boundary-layer method. *J. Fluids Eng.*, 1985, **107**, 428–430
7 McDonald, H. and Fish, R. W. Practical calculations of transitional boundary layers. *Int. J. Heat Mass Transfer*, 1973, **16**, 1729–1744
8 Cebeci, T. and Chang, K. C. Calculation of incompressible rough-wall boundary layer flows. *AIAA J.*, 1978, **16**, 730–735
9 Ligrani, P. M., Kays, W. M., and Moffat, R. J. A heat transfer prediction method for turbulent boundary layers developing over rough surfaces with transpiration. *Int. J. Heat Mass Transfer*, 1981, **24**(4), 774–778
10 Finson, M. L. A Reynolds stress model for boundary layer transition with application to rough surfaces. Physical Sciences Inc., MA, USA, Report PSI TR-34, 1975
11 Finson, M. L. On the application of second-order closure models to boundary layer transition. AGARD Committee Proceedings, AGARD-CP-224, 1977
12 Finson, M. L. A model for rough wall turbulent heating and skin friction. AIAA 20th Aerospace Meeting, Paper 82-0199, 1982
13 Finson, M. L. and Clarke, A. S. The effect of surface roughness on turbulent re-entry heating. AIAA Paper 80-1459, 1980
14 Finson, M. L. and Wu, P. K. S. Analysis of rough wall turbulent heating with application to blunted flight vehicles. AIAA Paper 79-008, 1979
15 Lin, T. C. and Bywater, R. J. Turbulence models for high-speed, rough-wall boundary layers. *AIAA J.*, 1982, **20**(3), 325–333
16 Christoph, G. H. and Pletcher, R. H. Prediction of rough-wall skin friction and heat transfer. *AIAA J.*, 1983, **21**(4), 509–515
17 Taylor, R. P., Coleman, H. W., and Hodge, B. K. Prediction of turbulent rough-wall skin friction using a discrete element approach. *J. Fluids Eng.*, 1985, **107**, 251–257
18 Feindt, E. G. Investigation on the dependence of laminar-turbulent transition on surface roughness and pressure gradient, *Schiffbautechnischen Geselschaft Jahrbach*, 1956, **50**
19 Taylor, R. P., Scaggs, W. F., and Coleman, W. W. Measurement and prediction of the effects of nonuniform surface roughness on turbulent flow friction coefficients. *J. Fluids Eng.*, 1988, **110**, 380–384
20 Grigson, C. The full-scale viscous drag of actual ship surfaces and the effect of quality of roughness on predicted power. *J. Ship Research*, 1987, **31**(3), 189–206
21 Tarada, F. Heat transfer to rough turbine blading. Ph.D. thesis, University of Sussex, 1987
22 Chien, K. Y. Predictions of channel and boundary-layer flows with a low-Reynolds-number turbulence model. *AIAA J.*, 1982, **20**(1), 33–38
23 Cebeci, T. and Smith, A. M. O. *Analysis of Turbulent Boundary Layers*. Academic Press, New York, 1974

Table 8 Model II results

Surface	α	γ	λ	H (mm)	L (mm)	$1/L_c^{1/2}$	$H/\bar{D}$
Acharya *et al.*, SRS1	0.995	1.85	27.6	0.345	0.616	6.11	0.101
Acharya *et al.*, SRS2	0.716	5.72	15.4	0.399	6.146	5.69	0.136

24 Marshall, J. K. Drag measurements in roughness arrays of varying density and distribution. *Agri. Meteorol.*, 1971, **8**, 269–292

25 Chen, C. K. Characteristics of turbulent flow resistance in pipes roughened with hemispheres. Ph.D. dissertation, Washington State University, 1971

26 Gaudet, L. Measurement of the drag of various three dimensional excrescences in turbulent boundary layers. Royal Aircraft Establishment Technical Report 85068 (England), 1985; also Aeronautical Journal, Paper No. 1484, April 1987, 170–182 (in abridged form)

27 Zukauskas, A. Heat transfer from tubes in cross-flow. *Advances in Heat Transfer*, vol. 18 (J. P. Harnett and F. I. Irvine, Jr., eds.), Academic Press, Orlando, 1987

28 Scaggs, W. F., Taylor, R. P., and Coleman, H. W. Measurement and prediction of rough wall effects on friction factors in turbulent pipe flow. Report TFD-88-1, Mech. Eng. Dept., Mississippi State University, 1988; also *J. Fluids Eng.*, 1988, **110**, 385–391

29 Morris, H. M. Flow in rough conduits. *Trans. ASCE*, 1955, **120**, 373–398

30 Coleman, H. W., Hodge, B. K., and Taylor, R. P. A re-evaluation of Schlichting's surface roughness experiment. *J. Fluids Eng.*, 1984, **106**, 60–65

31 Winter, K. G. and Gaudet, L. Turbulent boundary-layer studies at high Reynolds numbers at Mach numbers between 0.2 and 2.8. ARC R&M 3712, 1970

32 Rodi, W. and Scheuerer, G. Calculation of heat transfer to convection-cooled gas turbine blades. *J. Eng. Gas Turbines and Power*, 1985, **107**, 620–627

33 Karlsson, R. I. The effect of irregular surface roughness on the frictional resistance of ships. *Proc. Int. Symp. Ship Research*, SSPA, Goteburg, 1978, 9:1–9:20

34 Al-Shukri, S. M. The effect of sandpaper-type roughness on boundary-layer transition for turbomachinery blades. Ph.D. thesis, University of Liverpool, 1983

35 Acharya, M., Bornstein, J., and Escudier, M. P. Turbulent boundary layers on rough surfaces. *Expts. Fluids*, 1986, **4**, 33–47

36 Watt, R. M. Effects of surface roughness on the boundary-layer characteristics of turbine aerofoils. Ph.D. thesis, University of Oxford, 1988

37 Zukauskas, A. Heat transfer from tubes in cross-flow. *Advances in Heat Transfer*, vol. 8 (J. P. Harnett and T. F. Irvine, Ed.), Academic Press, New York, 1972

Appendix: Topographic models I and II

Topographic model I (truncated cones)

Melt-down height (h)

$$\beta=\frac{h}{H}=\frac{H^{-1}}{L_xL_z}\int_{z=0}^{L_z}\int_{x=0}^{L_x} y\,dx\,dz$$

$$=\frac{\pi}{12}\frac{D_0^2}{L_xL_z}(1+\gamma+\gamma^2)(1-\alpha\varepsilon) \tag{A1}$$

Centerline average value (R_a)

$$\frac{R_a}{H}=\frac{H^{-1}}{L_xL_z}\int_{z=0}^{L_z}\int_{x=0}^{L_x}|y'|\,dx\,dz$$

$$=f_1(\alpha,\beta,\gamma,\varepsilon)$$

$$y'=y-h$$

$$f_1=\frac{6\beta}{(1+\gamma+\gamma^2)(1-\alpha\varepsilon)}\left\{\tfrac{1}{6}(1+\gamma+\gamma^2)-\frac{\beta}{2}+\beta^2(1-\gamma)-\frac{\beta^3}{3}(1-\gamma)^2\right.$$
$$+\varepsilon\left[(\alpha+\beta)\frac{\gamma^2}{2}+\tfrac{1}{2}(\alpha+\beta(1-\gamma))(1+\gamma)-\frac{\alpha}{3}(1+\gamma+\gamma^2)\right]$$
$$\left.+\tfrac{1}{6}(1+\gamma+\gamma^2)(1-\alpha\varepsilon)-\frac{\beta}{2}(1+\varepsilon)\right\} \tag{A2}$$

High-order moment statistics ($n\geq 2$)

$$f_n(\alpha,\beta,\gamma,\varepsilon)=\frac{H^{-n}}{L_xL_z}\int_{z=0}^{L_z}\int_{x=0}^{L_x}(y')^n\,dx\,dz$$
$$=\frac{6\beta}{(1+\gamma+\gamma^2)(1-\alpha\varepsilon)}\left\{(1-\beta)^n\frac{\gamma^2}{2}\right.$$
$$+(1-\gamma)\left[\frac{(-1\beta^{n+1}}{n+1}\left(1-\frac{\beta(1-\gamma)}{n+2}\right)\right.$$
$$\left.+\frac{(1-\beta)^{n+1}}{n+1}\left(\gamma+\frac{(1-\gamma)(1-\beta)}{n+2}\right)\right]$$
$$+(-1)^n\varepsilon\left[(\beta+\alpha)\frac{\gamma^2}{2}\right.$$
$$+(1-\gamma)\left\{\frac{1}{\alpha(n+1)}(\gamma(\beta+\alpha)^{n+1}-\beta^{n+1})\right.$$
$$\left.\left.+\frac{1-\gamma}{\alpha^2(n+1)(n+2)}((\beta+\alpha)^{n+2}-\beta^{n+2})\right\}\right]$$
$$\left.+(-\beta)^n\left[\frac{1}{6\beta}(1+\gamma+\gamma^2)(1-\alpha\varepsilon)-\frac{1+\varepsilon}{2}\right]\right\} \tag{A3}$$

Arithmetic mean absolute profile slope value (m_a)

$$m_a=\frac{1}{L_xL_z}\int_{z=0}^{L_z}\int_{x=0}^{L_x}\left[\left(\frac{\partial y}{\partial x}\right)^2+\left(\frac{\partial y}{\partial z}\right)^2\right]^{1/2}dx\,dz$$
$$=\frac{6\beta}{(1+\gamma+\gamma^2)(1-\alpha\varepsilon)}\left(\frac{H}{D_0}\right)(1+\gamma)(1+\alpha\varepsilon^{1/2}) \tag{A4}$$

Root-mean-square profile slope value (m_q)

$$m_q=\left\{\frac{1}{L_xL_z}\int_{z=0}^{L_z}\int_{x=0}^{L_x}\left[\left(\frac{\partial y}{\partial x}\right)^2+\left(\frac{\partial y}{\partial z}\right)^2\right]dx\,dz\right\}^{1/2}$$
$$=2\left(\frac{H}{D_0}\right)\left[\frac{3\beta}{(1+\gamma+\gamma^2)(1-\alpha\varepsilon)}\left(\frac{1+\gamma}{1-\gamma}\right)(1+\alpha^2)\right]^{1/2} \tag{A5}$$

Arithmetic mean absolute angle value (ϕ_a)

$$\phi_a=\frac{1}{L_xL_z}\int_{z=0}^{L_z}\int_{x=0}^{L_x}\arctan\left[\left(\frac{\partial y}{\partial x}\right)^2+\left(\frac{\partial y}{\partial z}\right)^2\right]^{1/2}dx\,dz$$
$$=\frac{3\beta}{(1+\gamma+\gamma^2)(1-\alpha\varepsilon)}(1-\gamma^2)\left[\arctan(R)+\varepsilon\arctan\left(\frac{\alpha R}{\varepsilon^{1/2}}\right)\right] \tag{A6}$$

where

$$R=\frac{2}{1-\gamma}\left(\frac{H}{D_0}\right)$$

Root-mean-square angle value (ϕ_q)

$$\phi_q=\left\{\frac{1}{L_xL_z}\int_{z=0}^{L_z}\int_{x=0}^{L_x}\left[\arctan\left(\left(\frac{\partial y}{\partial x}\right)^2+\left(\frac{\partial y}{\partial z}\right)^2\right)^{1/2}\right]^2dx\,dz\right\}^{1/2}$$
$$=\left\{\frac{3\beta}{(1+\gamma+\gamma^2)(1-\alpha\varepsilon)}(1-\gamma^2)\right.$$
$$\left.\times\left[(\arctan R)^2+\varepsilon\left(\arctan\left(\frac{\alpha R}{\varepsilon^{1/2}}\right)\right)^2\right]\right\}^{1/2} \tag{A7}$$

Topographic model II (spherical segments)

Melt-down location (h)

$$\beta=\frac{h}{H}=\frac{\pi H^2}{L_x L_z}\left[\lambda-\tfrac{1}{3}-\alpha^2\left(\gamma-\frac{\alpha}{3}\right)\right] \tag{A8}$$

Centerline average value (R_a)

$$\frac{R_a}{H}=f_1(\alpha,\beta,\gamma,\lambda) \tag{A9}$$

where

$$\begin{aligned} f_1=\frac{2\beta}{\lambda-1/3-\alpha^2(\gamma-\alpha/3)}\Bigg\{&\frac{(1-\beta)^3}{3}\\ &+(\beta+\lambda-1)\frac{(1-\beta)^2}{2}+(2\beta-\gamma+\alpha+\lambda-1)\frac{\beta^2}{2}\\ &+\frac{(\beta+\alpha)^3}{3}+(\gamma-\beta-\alpha)\frac{(\beta+\alpha)^2}{2}\\ &+\tfrac{1}{2}[\lambda-\tfrac{1}{3}-\alpha^2(\gamma-\alpha/3)]-\frac{\beta}{2}[\gamma^2-(\gamma-\alpha)^2+\lambda^2-(\lambda-1)^2]\Bigg\} \end{aligned}$$

High-order moment statistics ($n\geq 2$)

$$\begin{aligned} f_n=\frac{2\beta}{\lambda-1/3-\alpha^2(\gamma-\alpha/3)}\Bigg\{&\frac{(1-\beta)^{n+2}}{n+2}\\ &+(\beta+\lambda-1)\frac{(1-\beta)^{n+1}}{(n+1)}+2(-1)^{n+1}\left(\frac{\beta^{n+2}}{n+2}\right)\\ &+(-1)^n\frac{(\beta+\alpha)^{n+2}}{n+2}-(\gamma-\beta-\alpha)(-1)^{n+1}\frac{(\beta+\alpha)^{n+1}}{n+1}\\ &+(-2\beta-\lambda+1+\gamma-\alpha)\frac{(-\beta)^{n+1}}{n+1}\\ &+(-\beta)^n\Bigg[\frac{1}{2\beta}(\lambda-\tfrac{1}{3}-\alpha^2(\gamma-\alpha/3))\\ &-\tfrac{1}{2}(\gamma^2-(\gamma-\alpha)^2+\lambda^2-(\lambda-1)^2)\Bigg]\Bigg\} \end{aligned} \tag{A10}$$

Arithmetic mean absolute profile slope value (m_a)

$$m_a=\frac{2\beta}{\lambda-1/3-\alpha^2(\gamma-\alpha/3)}[\lambda^2(\sec^2\theta_0-1)+\gamma^2(\sec^2\theta_1-1)] \tag{A11}$$

where

$$\theta_0=\arcsin[\lambda^{-1}(2\lambda-1)^{1/2}]$$

$$\theta_1=\arcsin[\gamma^{-1}(2\gamma\alpha-\alpha^2)^{1/2}]$$

Root-mean-square profile slope value (m_q)

$$\begin{aligned} m_q=\Bigg\{&\frac{\beta}{\lambda-1/3-\alpha^2(\gamma-\alpha/3)}[-v_0^2\ln(\lambda^2-v_0^2)\\ &-(\lambda^2-v_0^2)(\ln(\lambda^2-v_0^2)-1)\\ &+\lambda^2(\ln\lambda^2-1)-v_1^2\ln(\gamma^2-v_1^2)\\ &-(\gamma^2-v_1^2)(\ln(\gamma^2-v_1^2)-1)+\gamma^2(\ln\gamma^2-1)]\Bigg\}^{1/2} \end{aligned} \tag{A12}$$

where

$$v_0=(2\lambda-1)^{1/2}$$

$$v_1=(2\gamma\alpha-\alpha^2)^{1/2}$$

Arithmetic mean absolute angle value (ϕ_a)

$$\begin{aligned} \phi_a=\frac{\beta}{4[\lambda-1/3-\alpha^2(\gamma-\alpha/3)]}&[\lambda^2(\sin 2\theta_0-2\theta_0\cos 2\theta_0)\\ &+\gamma^2(\sin 2\theta_1-2\theta_1\cos 2\theta_1)] \end{aligned} \tag{A13}$$

Root-mean-square angle value (ϕ_q)

$$\begin{aligned} \phi_q=\Bigg\{&\frac{\beta}{\lambda-1/3-\alpha^2(\gamma-\alpha/3)}\Bigg[\lambda^2\left(\frac{\theta_0}{2}\sin 2\theta_0\right.\\ &\left.-\frac{\theta_0^2}{2}\cos 2\theta_0+\tfrac{1}{4}(\cos 2\theta_0-1)\right)\\ &+\gamma^2\left(\frac{\theta_1}{2}\sin 2\theta_1-\frac{\theta_1^2}{2}\cos 2\theta_1+\tfrac{1}{4}(\cos 2\theta_1-1)\right)\Bigg]\Bigg\}^{1/2} \end{aligned} \tag{A14}$$